TÜBİTAK

Turkish Journal of Electrical Engineering & Computer Sciences

http://journals.tubitak.gov.tr/elektrik/

Research Article

Turk J Elec Eng & Comp Sci
(2018) 26: 3192 – 3206
© TÜBİTAK
doi:10.3906/elk-1707-124

Controlling the speed and flux of a dual stator winding induction motor using an emotional intelligent controller and integration algorithm

Hojat MOAYEDIRAD, Mohammad Ali SHAMSI-NEJAD*
Faculty of Electrical and Computer Engineering, University of Birjand, Birjand, Iran

Received: 11.07.2017 • **Accepted/Published Online:** 29.05.2018 • **Final Version:** 29.11.2018

Abstract: The appropriate efficiency of a dual stator winding squirrel-cage induction motor (DSWIM) is obtained when the ratio of two frequencies feeding the machine is equal to the ratio of the number of poles. In the vector control method, the estimation of flux at low speed is difficult. To solve this problem, researchers have benefited from the free capacity of the two windings of the stator. This makes the motor deviate from its standard operating mode at low speed. The main purpose of the present study is to reduce the power losses of the inverter units in the sensorless DSWIM drive using the proposed control scheme at low speed. In this control scheme, the speed is estimated based on the modified intelligent model reference adaptive system (MIMRAS) without estimating the stator resistance at low speed. The proposed methods were simulated in MATLAB/Simulink software, and the results of simulation confirmed the assumptions.

Key words: Dual stator winding, induction motor, intelligent model reference adaptive system, low speed, sensorless

1. Introduction

The dual stator winding induction motor (DSWIM) studied in this paper consists of a standard squirrel-cage rotor and a stator with two separate symmetric three-phase windings with different numbers of poles. Each stator winding is fed by an independent inverter through a common dc-bus. The DSWIM was introduced by Muñoz and Lipo [1]. Due to having two independent inverters and two separate symmetric three-phase windings, a DSWIM drive has better reliability than a three-phase induction motor (IM) drive. Generally, the poles of the stator are chosen in the ratio of 1 to 3 (e.g., 2:6 or 4:12). The standard operating mode of a DSWIM is obtained when the ratio of two frequencies feeding the machine is equal to the ratio of the number of poles [1–3]. The most common method of speed control in the IMs is the vector control method [4]. The direct and indirect vector control methods depend on flux estimation [4–6]. There are two direct vector control methods: the voltage and current models. The voltage model depends on stator resistance. In the indirect vector control method, the calculation of the slip frequency depends on the rotor resistance. In the direct vector control, at low speed, the estimation of flux has noticeable sensitivity because the voltage drop on the stator resistance is comparable to the input stator voltage. In [6], the rotor resistance was estimated using a novel Flux-MRAS scheme based on artificial neural network in the indirect vector control method. In [7–9], the stator resistance estimation was utilized to solve the speed estimation problem of the IM at low speed. In [10,11], different kinds of reformed extended Kalman filter (EKF) algorithms were presented for improving flux and torque estimation.

*Correspondence: mshamsi@birjand.ac.ir

Due to high complexity, computation time is long. In [12], an IM flux estimation method was proposed based on a new integration method with a closed loop DC offset compensation algorithm. This method estimates an exact flux only when the system parameters are known. In [13], a modified MRAS based on particle swarm optimization (PSO) was proposed for speed estimation. Due to high complexity and long computation time, PSO is unsuitable for on-line estimation in real time. In [14], the backstepping control technique was presented based on the MRAS approach for sensorless speed control of an IM. Due to uncertain stator resistance, it is not suitable at low speed. Based on conventional control methods, a DSWIM drive in its standard operating mode cannot properly trace low speed. In the method proposed in [1], one of the windings is fed by an arbitrary constant frequency (usually 0.05 p.u.) and the other one is fed by a variable frequency. This operating mode forces the low-pole winding to produce a torque larger than the mechanical load. In other words, unlike the first winding, the second one can produce negative and positive torques dependent upon the desired speed and torque. Consequently, by enforcing the first winding to work at an arbitrary constant frequency, the motor deviates from its standard operating mode, but the problem of drive for tracing low speed is solved. The vector control methods presented in [15,16] are based on the seminal method presented in [1]. The conventional control method leads to the loss of optimal energy management at low speed in a DSWIM. The proper efficiency of this motor is obtained when it works in its standard operating mode [2]. In [5], a rotor flux compensator was used to solve the problem of estimating the rotor flux of an IM drive at low speed. This perfectly solved the problem of the rotor flux estimation at low speed without estimating the stator resistance. In the present study, the following were performed: 1. The vector control method was first presented based on the rotor flux compensation method. 2. The MIMRAS was proposed for estimating the rotor speed in the proposed DSWIM drive. At low speed, the loss of the motor core was not significant [17]. The main purpose of the present study was to reduce the inverter loss in the sensorless DSWIM drive using the proposed ideas at low speed. The paper is organized as follows: A model of the DSWIM is presented in Section 2. The proposed vector control of the DSWIM drive using MIMRAS is explained in Section 3. Results and discussions are given in Section 4, and finally, the conclusion is presented in Section 5.

2. Machine model

The d-q equations of the voltage in a dual stator winding induction motor with different numbers of poles can be expressed in complex form as in Eqs. (1) and (2) [1]:

$$V_{qdsi} = R_{si} i_{qdsi} + \rho \lambda_{qdsi} - j\omega \lambda_{qdsi}, \tag{1}$$

$$V_{qdri} = R_{ri} i_{qdri} + \rho \lambda_{qdri} - j(\omega - \omega_{ri)} \lambda_{qdri} = 0, \tag{2}$$

where i can be 1 or 2, presenting the parameters and state variables of each three-phase stator winding ($abc1$ and $abc2$). ω is the electrical rotating speed of the common reference frame; ω_{ri} is the rotor electrical speed; V_{qdsi} and V_{qdri} are the stator and rotor voltages on the q- and d-axis, respectively; i_{qdsi} and i_{qdri} are the stator and rotor currents on the q- and d-axis, respectively; λ_{qdsi} and λ_{qdri} are stator and rotor flux linkages on the q- and d-axis, respectively; R_{si} and R_{ri} are stator and rotor resistances, respectively, and $\rho = d/dt$. Flux linkage equations given in terms of currents are provided in Eq. (3) [1]:

$$\begin{bmatrix} \lambda_{qdsi} \\ \lambda_{qdri} \end{bmatrix} = \begin{bmatrix} L_{si} & L_{mi} \\ L_{mi} & L_{ri} \end{bmatrix} \times \begin{bmatrix} i_{qdsi} \\ i_{qdri} \end{bmatrix}, \tag{3}$$

where L_{ri} and L_{si} are the rotor and stator inductances, L_{mi} is the magnetizing inductance (see Figure 1). From Eq. (3), the stator and rotor currents can be expressed in terms of flux linkages as in Eqs. (4) and (5) [18]:

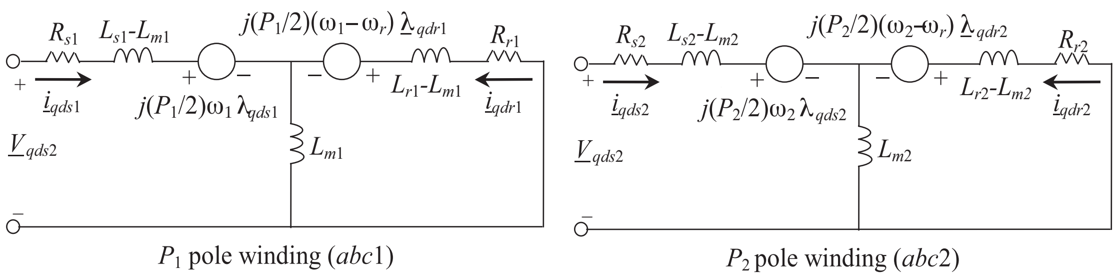

Figure 1. Complex vector control of dual stator winding squirrel-cage induction motor.

$$i_{qdsi} = \frac{L_{ri}}{D_i}\lambda_{qdri} - \frac{L_{mi}}{D_i}\lambda_{qdri}, \tag{4}$$

$$i_{qdri} = \frac{L_{si}}{D_i}\lambda_{qdri} - \frac{L_{mi}}{D_i}\lambda_{qdsi}, \tag{5}$$

where $D_i = L_{si}L_{ri} - L_{mi}^2$. By Substituting Eq. (4) into Eq. (1), and Eq. (5) into Eq. (2), the voltage equations become Eqs. (6) and (7). The electromagnetic torque (T_{ei}) for each stator winding is given in complex variable form in Eq. (8):

$$V_{qdsi} = \frac{R_{si}L_{ri}}{D_i}\lambda_{qdsi} - \frac{R_{si}L_{mi}}{D_i}\lambda_{qdri} + p\lambda_{qdsi} - j\omega\lambda_{qdsi}, \tag{6}$$

$$0 = \frac{R_{ri}L_{si}}{D_i}\lambda_{qdsi} - \frac{R_{ri}L_{mi}}{D_i}\lambda_{qdsi} + p\lambda_{qdri} - j(\omega - \omega_{ri})\lambda_{qdri}, \tag{7}$$

$$T_{ei} = \frac{3}{2}\frac{P_i}{2}\mathrm{Im}(\lambda_{qdsi}\, i_{dqsi}^*), \tag{8}$$

where P_i is the pole number for windings, $i = 1$ or 2. The total electromagnetic torque (T_e) of a DSWIM is the sum of produced torques via both stator windings, which is given in Eq. (9) [18]. The rotor electrical speed (ω_{ri}) can be defined in terms of the rotor mechanical speed (ω_r) as in Eq. (10) [16]. The air-gap flux linkage is expressed in Eq. (11). The currents are eliminated by substituting Eqs. (4) and (5) into Eq. (11). Therefore, the air-gap flux linkage of each stator winding can be stated in terms of rotor and stator flux linkages as in Eq. (12). The total air-gap flux linkage is the sum of the two separate air-gap flux linkages, which is defined in Eq. (13):

$$T_e = T_{e1} + T_{e2} = \frac{3}{2}\frac{P_1}{2}\mathrm{Im}(\lambda_{qds1}\, i_{dqs1}^*) + \frac{3}{2}\frac{P_2}{2}\mathrm{Im}(\lambda_{qds2}\, i_{dqs2}^*), \tag{9}$$

$$\omega_{ri} = \frac{P_i}{2}\omega_r, \tag{10}$$

$$\lambda_{qdmi} = L_{mi}i_{qdsi} + L_{mi}i_{qdri}, \tag{11}$$

$$\lambda_{qdmi} = \frac{L_{lri}L_{mi}}{D_i}\lambda_{qdsi} + \frac{L_{lsi}L_{mi}}{D_i}\lambda_{qdri}, \tag{12}$$

$$\lambda_{qdm} = \frac{L_{lr1}L_{m1}}{D_1}\lambda_{qds1} + \frac{L_{ls1}L_{m1}}{D_1}\lambda_{qdr1} + \frac{L_{lr2}L_{m2}}{D_2}\lambda_{qds2} + \frac{L_{ls2}L_{m2}}{D_2}\lambda_{qdr2}. \tag{13}$$

The mechanical equation of the machine is explained in Eq. (14):

$$p\omega_r = \frac{K_{e1}}{J}(\lambda_{dr1}I_{qs1} - \lambda_{qr1}I_{ds1}) + \frac{K_{e2}}{J}(\lambda_{dr2}I_{qs2} - \lambda_{qr2}I_{ds2}) - \frac{T_L}{J}, \tag{14}$$

where J is the inertia coefficient, $K_{e1} = (3P_1/4)(L_{m1}/L_{r1})$, and $K_{e2} = (3P_2/4)(L_{m2}/L_{r2})$. In [1], it is proved theoretically and experimentally that both stator windings in the DSWIM are fully decoupling. The equivalent circuit diagram of a DSWIM, using $d-q$ notation, is shown in Figure 1 [1]. The low-pole number winding is referred to as $abc1$ and the high-pole number winding as $abc2$.

3. The proposed vector control of the sensorless DSWIM drive

A DSWIM is similar to two independent three-phase IMs that are mechanically coupled. Therefore, speed control methods used for three-phase IMs are also applicable to a DSWIM [1–3]. In the vector control method, Eqs. (15)–(21) are utilized for generating feedback signals [1,19]:

$$\varphi^s_{dqsi} = \int (v^s_{dqsi} - R_{si}i^s_{dqsi})dt, \tag{15}$$

$$\varphi^s_{qdmi} = \varphi^s_{qdsi} - L_{lsi}i^s_{qdsi}, \tag{16}$$

$$\varphi^s_{dqri} = (L_{ri}/L_{mi})\varphi^s_{dqmi} - L_{lri}i^s_{dqsi}, \tag{17}$$

$$T_{ei} = (3P_i/4)(\varphi^s_{dsi}i^s_{qsi} - \varphi^s_{qsi}i^s_{dsi}), \tag{18}$$

$$\varphi_{ri} = \sqrt{(\varphi^s_{qri})^2 + (\varphi^s_{dri})^2}, \tag{19}$$

$$\cos\theta_{ei} = \varphi^s_{dri}/\varphi_{ri}, \tag{20}$$

$$\sin\theta_{ei} = \varphi^s_{qri}/\varphi_{ri}. \tag{21}$$

where φ^s_{dqsi}, φ^s_{dqri}, and φ^s_{dqmi} are the stator, rotor, and air-gap d- and q-axis fluxes, respectively; L_{lsi} and L_{lri} are the stator and rotor leakage inductances, respectively. The block diagram of the proposed sensorless DSWIM drive using the voltage model of the direct vector control is shown in Figure 2, where K_1 and K_2 are the torque-sharing factor and the flux coefficient; $\hat{\omega}_r$ and $\Delta\omega_r$ are the estimated speed and the speed error, respectively. In Figure 2, the MIMRAS has been modeled as biobjective.

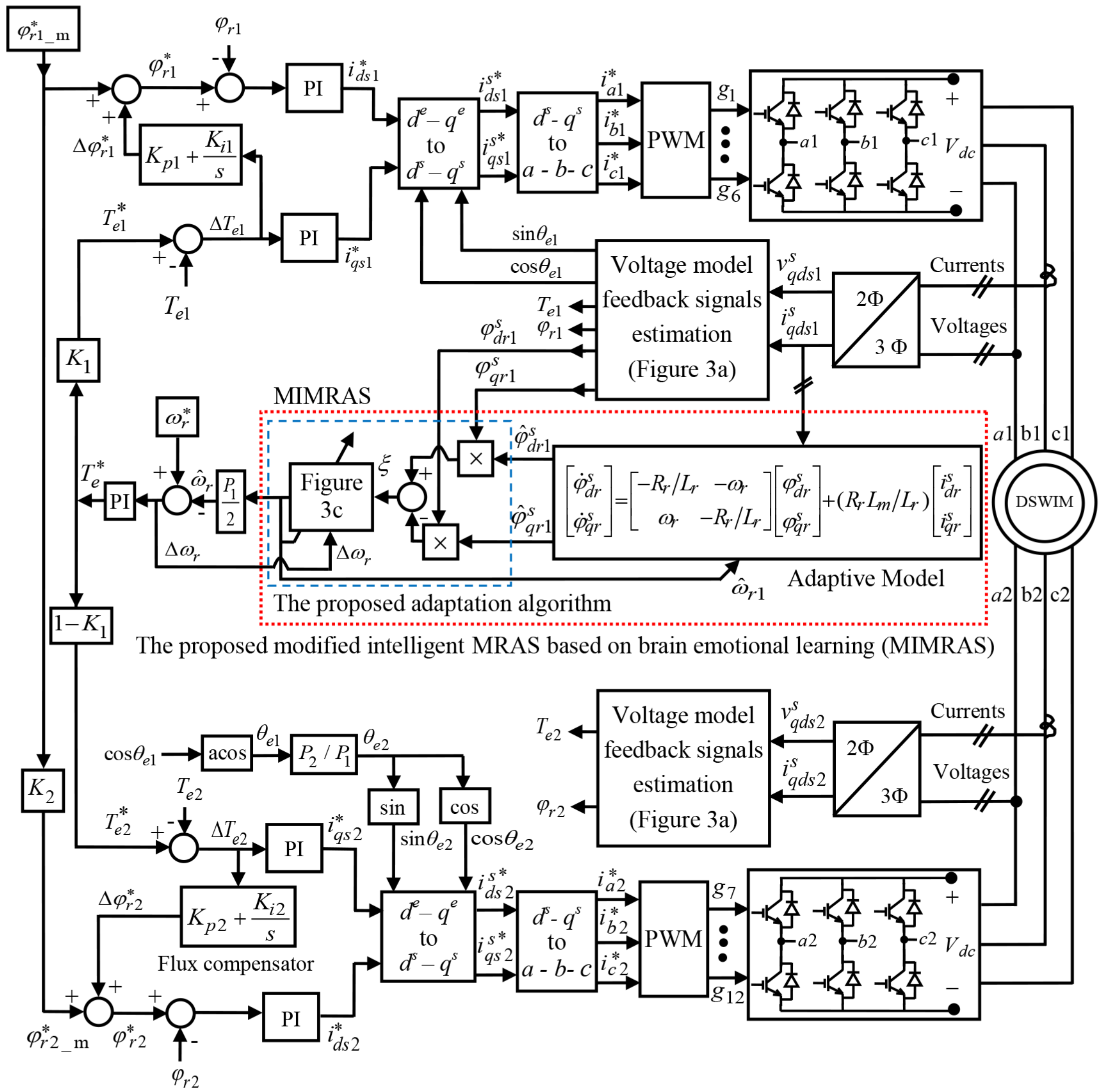

Figure 2. The block diagram of the proposed control scheme of the sensorless DSWIM drive based on the MIMRAS method.

3.1. Voltage model feedback signals estimation

The rotor flux, the electromagnetic torque, $\sin\omega_{ei}t$ and $\cos\omega_{ei}t$ signals are estimated from the block diagram in Figure 3a. From Eq. (15), the stator flux in the drive control system of a DSWIM is directly obtained by integrating the electromotive force. The pure integrator has the problem of DC offset. Instead, the algorithm presented in [20] is utilized. The block diagram of the integration algorithm is shown as dashed lines in Figure 3a.

3.2. Flux compensation model

In the direct vector control method, the estimation of $\sin\omega_{ei}t$ and $\cos\omega_{ei}t$ signals is dependent on the estimation of the rotor flux. At low speed, the voltage drop on stator resistance $(R_s i_s)$ is comparable with the input stator voltage (V_s). As a result, the rotor flux is low and it cannot drive the DSWIM, which makes the operation

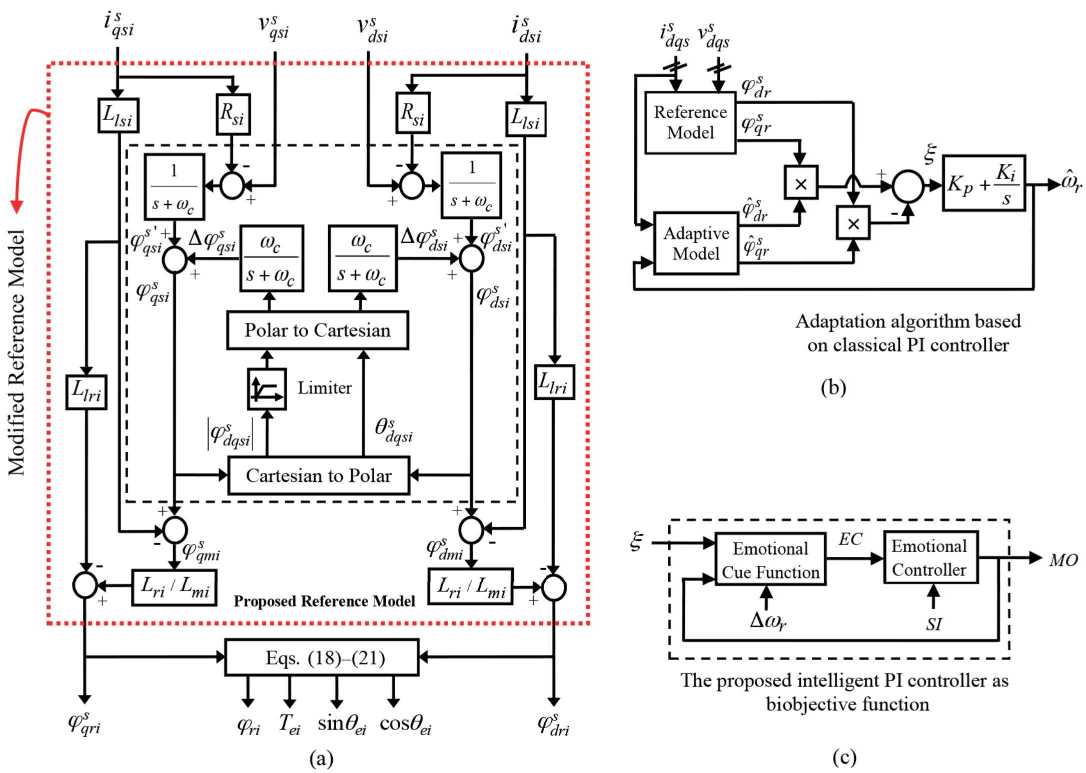

Figure 3. a) The block diagram of the estimation of voltage model feedback signals for the proposed sensorless DSWIM drive, b) A basic configuration of the speed estimator based on MRAS, and c) The structure of the proposed intelligent PI controller based on the brain emotional learning mechanism for the adaptation algorithm as the biobjective function ($\xi \to 0$ and $\Delta\omega_r \to 0$).

of the DSWIM drive difficult at low speed [5]. Most researchers estimate the stator resistance to compensate the voltage drop on the stator resistance [6–9]. The present study directly uses the torque error to compensate the rotor flux without estimating the stator resistance at low speed. If torque error always exists ($\Delta T_e \neq 0$), then the actual torque T_e is always less than the reference torque T_e^*. In this compensator, the rotor flux is compensated with a general proportional and integral (PI) controller whose input is the torque error. The rotor flux is compensated when the torque error (ΔT_e) exists. The main purpose of the control system in the DSWIM drive is to decrease the error of electromagnetic torque and consequently eliminate the speed error ($\Delta\omega_r \to 0$). At low speed, the estimated rotor flux ($\hat{\varphi}_{ri}$) is not equal to its actual value $\varphi_{ri}(\varphi_{ri} \neq \hat{\varphi}_{ri})$. It is proposed that $\Delta\varphi_{ri}^*$ is added to the main reference flux ($\varphi_{ri\_m}^*$) to make it a component of $\varphi_{ri}^* = \varphi_{ri\_\mathrm{m}}^* + \Delta\varphi_{ri}^*$. In this paper, a flux compensator generates $\Delta\varphi_{ri}^*$.

In the proposed control scheme for $T_e > 0$, total torque is defined as $T_e = T_{e1} + T_{e2} = |T_{e1}| + |T_{e2}|$, although it is defined as $T_e = T_{e1} + T_{e2} \neq |T_{e1}| + |T_{e2}|$ in the conventional method.

3.3. The speed estimation using the model referencing adaptive system based on the flux compensator and biobjective emotional intelligent controller

A speed estimator based on conventional MRAS is shown in Figure 3b [19]. The reference model in the conventional MRAS is defined in Eq. (22) [19]:

$$\begin{bmatrix} \dot{\varphi}_{dr}^s \\ \dot{\varphi}_{qr}^s \end{bmatrix} = (L_r/L_m)\left\{ \begin{bmatrix} v_{ds}^s \\ v_{qs}^s \end{bmatrix} - \begin{bmatrix} (R_s+\sigma L_s S) & 0 \\ 0 & (R_s+\sigma L_s S) \end{bmatrix} \begin{bmatrix} i_{ds}^s \\ i_{qs}^s \end{bmatrix} \right\}, \tag{22}$$

where $\sigma = 1 - L_m^2/L_sL_r$ is the leakage coefficient. A conventional MRAS has two problems at low speed: 1. Due to pure integrations and the voltage drop on the stator resistance, the rotor flux calculation in the reference model is difficult, especially at low speed [19]. For solving this problem, researchers usually estimate the stator resistance [6,7]; 2. To have a high performance and accuracy in sensorless DSWIM drive, particularly at low speed, adjusting K_p and K_i coefficients are important in the classical PI controller of the MRAS adaptation algorithm. The modified reference model in the MIMRAS is shown in Figure 3a. The MIMRAS has three features: 1. An integration algorithm presented in [20] is utilized instead of the pure integrator; 2. The rotor flux components of the reference model are calculated without estimating the stator resistance based on the rotor flux compensator; and 3. K_p and K_i coefficients in the proposed adaptation algorithm are adjusted using the brain emotional learning as single-objective and biobjective. The first objective is balancing the fluxes, $\xi \rightarrow 0$; in other words, $\varphi_{dr}^s = \hat{\varphi}_{dr}^s$ and $\varphi_{qr}^s = \hat{\varphi}_{qr}^s$. To have an accurate estimation of the speed at low speed, the speed error $(\Delta\omega_r \rightarrow 0)$ is defined as the second objective of the adaptation algorithm. Due to low complexity, the emotional intelligent controller is suitable for on-line application.

In this paper, one of the purposes is to use the computational model mentioned in [4,21] by expanding it with a novel intelligent control structure. An emotional intelligent model has two main sections: Amygdala (A) and Orbitofrontal Cortex (OC). Learning is done in the Amygdala unit. The Orbitofrontal Cortex is applied for reformatting responses and unsuitable reactions of the Amygdala. The emotional learning system response of Amygdala-Orbitofrontal (MO) to sensory input (SI) and emotional cue (EC) is given in Eq. (23):

$$MO = AO - OCO, \tag{23}$$

where AO and OCO are outputs of the Amygdala and the Orbitofrontal Cortex units, respectively. AO and OCO are defined in Eq. (24). The learning law in Amygdala and Orbitofrontal units are defined in Eqs. (25) and (26):

$$AO = G_a.SI, OCO = G_{oc}.SI, \tag{24}$$

$$\text{For Amygdala:} \Delta G_a = C_1.\max(0, EC - AO) \geq 0, \tag{25}$$

$$\text{ForOrbitofrontal Cortex:} \Delta G_{oc} = C_2.(MO - EC), \tag{26}$$

where G_a and G_{oc} are equivalent gains of the Amygdala and Orbitofrontal units, respectively. C_1 and C_2 are learning coefficients of the Amygdala and Orbitofrontal units, respectively. In Eq. (25), since the operator "max" is used in the learning law of Amygdala, the gain of the Amygdala unit always increases. The Amygdala unit cannot forget anything it has learned. The gain of the Orbitofrontal unit can be changed as positive or negative to reform well the unsuitable responses of the Amygdala unit [21]. Eq. (27) is written by compounding Eqs. (23) and (24). In the proposed MRAS, the intelligent controller is used as a PI controller. Therefore, SI is defined in Eq. (28):

$$MO = (G_a - G_{oc}).SI = G(SI, EC, ...).SI, \tag{27}$$

$$SI = K_p.\xi + K_i.\int_0^t \xi dt, \tag{28}$$

where K_p and K_i are proportional and integral coefficients, respectively, ξ is defined as balancing fluxes($\xi = \hat{\varphi}^s_{dr}\varphi^s_{qr} - \hat{\varphi}^s_{qr}\varphi^s_{dr}$). EC can be formulated based on required objectives [21]. In this paper, it is defined in Eqs. (29) and (30):

$$\text{Single-objectivefunction } (\xi \to 0){:}EC = a_{ec1}.\xi + a_{ec2}.MO, \tag{29}$$

$$\text{Bi-objectivefunction}(\xi \to 0 and \Delta\omega_r \to 0){:}EC = a_{ec1}.\xi + a_{ec2}.MO + a_{ec3}.\Delta\omega_r, \tag{30}$$

where a_{ec1}, a_{ec2}, and, a_{ec3} are input coefficients of EC function, $\Delta\omega_r$ is the rotor speed error. The proposed intelligent PI controller is shown in Figure 3c that is based on the emotional learning system of the brain Amygdala-Orbitofrontal.

At low speed, balancing fluxes is difficult and sensitive. In this paper, the intelligent PI controller of MRAS is adjusted as problem of the single-objective ($\xi \to 0$) and biobjective ($\xi \to 0$ and $\Delta\omega_r \to 0$). In the single-objective, the proposed MRAS estimates the rotor speed only based on balancing of rotor fluxes ($\xi \to 0$). The purpose of the main control system in the DSWIM drive is to reduce the speed error to zero. This purpose ($\Delta\omega_r \to 0$) is selected as the second objective in the PI controller of the MIMRAS. In fact, the value of $\Delta\omega_r$ is directly participated in the speed estimation. As a result, the convergence between $\hat{\omega}_r$ and ω^*_r is increased, which in turn reduces the speed estimation error particularly at low speed.

The direct vector control of the voltage model in DSWIM drive is independent of the rotor resistance. Estimations of $\hat{\varphi}^s_{qr}$ and $\hat{\varphi}^s_{dr}$ in the adaptive model of the MRAS are dependent upon rotor resistance as in Eqs. (31) and (32):

$$\hat{\varphi}^s_{qr} = (i^s_{ds}L_mR_r/L_r - \dot{\hat{\varphi}}^s_{qr} - \hat{\varphi}^s_{qr}R_r/L_r)\Big/\hat{\omega}_r, \tag{31}$$

$$\hat{\varphi}^s_{dr} = -(i^s_{qs}L_mR_r/L_r - \dot{\hat{\varphi}}^s_{dr} - \hat{\varphi}^s_{dr}R_r/L_r)\Big/\hat{\omega}_r, \tag{32}$$

where $\hat{\varphi}^s_{qr}$ and $\hat{\varphi}^s_{dr}$ are d- and q-axis estimated rotor fluxes via the adaptive model, respectively. In [22], it is mentioned that the robustness of the MRAS speed estimator to the rotor resistance variation depends on the value of PI controller coefficients (K_p and K_i) in the speed-adaptation loop. According to the results, the value of K_p and K_i coefficients of PI controller in the speed-adaptation loop are important and depends on the rotor resistance. In this paper, the value of K_p and K_i coefficients of PI controller in the speed-adaptation loop are adjusted using the brain emotional learning as biobjective. In the MIMRAS, the brain emotional learning is a suitable method for adjusting the PI controller coefficients. From Eqs. (31) and (32), the normalized sensitivity functions of $\hat{\varphi}^s_{qr}$ and $\hat{\varphi}^s_{dr}$ to rotor resistance in the adaptive model of the MIMRAS ($S^{\hat{\varphi}^s_{qr1}}_{R_{r1}}, S^{\hat{\varphi}^s_{dr1}}_{R_{r1}}$) can be expressed as in Eqs. (33) and (34), respectively:

$$S^{\hat{\varphi}^s_{qr1}}_{R_{r1}} = \frac{\partial\hat{\varphi}^s_{qr1}/\hat{\varphi}^s_{qr1}}{\partial R_{r1}/R_{r1}} = [R_{r1}/(L_{r1}\hat{\varphi}^s_{qr1}\hat{\omega}_r)][L_{m1}i^s_{ds1} - \hat{\varphi}^s_{dr1}), \tag{33}$$

$$S^{\hat{\varphi}^s_{dr1}}_{R_{r1}} = \frac{\partial\hat{\varphi}^s_{dr1}/\hat{\varphi}^s_{dr1}}{\partial R_{r1}/R_{r1}} = [R_{r1}/(L_{r1}\hat{\varphi}^s_{dr1}\hat{\omega}_r)][\hat{\varphi}^s_{qr1} - L_{m1}i^s_{qs1}), \tag{34}$$

where $\hat{\omega}_r$ is the estimated rotor speed using the biobjective emotional intelligent controller. In Section 4, the sensitivity of $\hat{\varphi}^s_{qr}$ and $\hat{\varphi}^s_{dr}$ to rotor resistance in the adaptive model of the MIMRAS is studied.

4. Results and discussions

The simulation of the dual stator winding squirrel-cage induction motor drive was performed in MATLAB/Simulink to evaluate the proposed ideas. The parameters of the sensorless DSWIM drive are given in the appendix [2,4]. The parameters of the utilized IGBT/Diode were selected from SKM40GD123D IGBT. The simulation was run in the following two models:

1. The conventional control model of a DSWIM drive (the conventional method),
2. The proposed control model of the sensorless DSWIM drive (the proposed method).

4.1. Simulation results of the conventional method

In the conventional model, the frequency is usually held constant at a minimum value in the first winding, the second winding can work in either motor or generator operating mode at low speed. In other words, the algebraic sum of the torques produced by $abc1$ and $abc2$ windings has to be equal to the requested torque. Figure 4 demonstrates the behavior of the conventional drive control system of a DSWIM in response to the speed command of 0.4 rad/s with the load torque value of 2 N.m. The drive control system perfectly traces the low reference speed in the steady state. Figure 4b shows the total torque (T_e) and the profile of the torque produced by $abc1$ and $abc2$ windings (T_{e1} and T_{e2}). T_e is obtained from the sum of T_{e1} and T_{e2} ($T_e = T_{e1} + T_{e2}$).

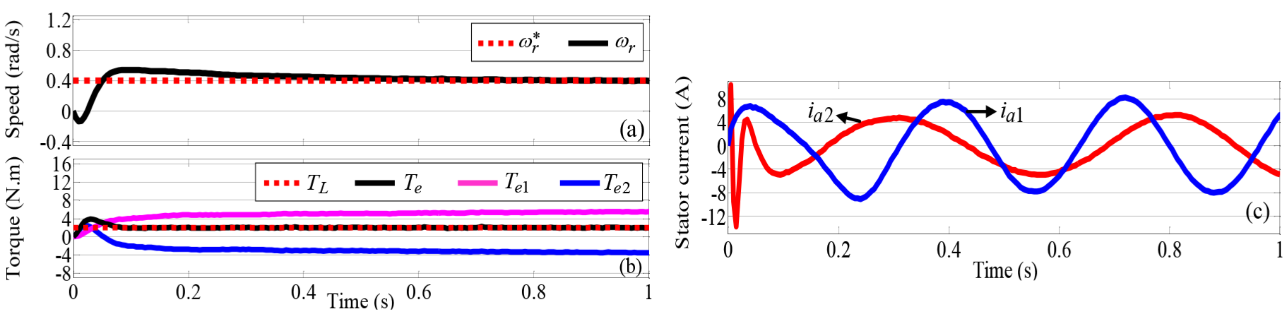

Figure 4. Simulation results of the conventional drive control system of DSWIM. The reference speed is 0.4 rad/s and the torque value is 2 N.m. a) Rotor speed profile, b) Torque profile, and c) Stator currents i_{a1} and i_{a2}.

4.2. Simulation results of the proposed control scheme

Figure 5 illustrates the behavior of the proposed control system of the sensorless DSWIM drive based on the proposed biobjective intelligent MRAS. The reference speed changes from 9 to 0.4 rad/s, the load torque drops from 4 to 2 N.m. The drive control system perfectly traces low reference speeds in the steady state. Figure 5b shows the total torque (T_e) and the profile of the torque produced by $abc1$ and $abc2$ windings (T_{e1} and T_{e2}). T_e is calculated from the sum of T_{e1} and T_{e2} ($T_e = T_{e1} + T_{e2}$). Each of the torques produced by stator windings makes a percentage of the total torque, and the sum of the percentages does not exceed 100. This is an important feature of the standard operating mode of this motor. Figure 5c depicts the estimated rotor fluxes via the voltage model in the proposed DSWIM drive. In addition, the phase currents of $a1$ and $a2$ are shown in Figure 5d.

Figure 6 shows the behavior of the proposed sensorless DSWIM drive in response to the speed command of 2 rad/s with the load torque value of 1 N.m. Figure 6a shows the behavior of the proposed MRAS based

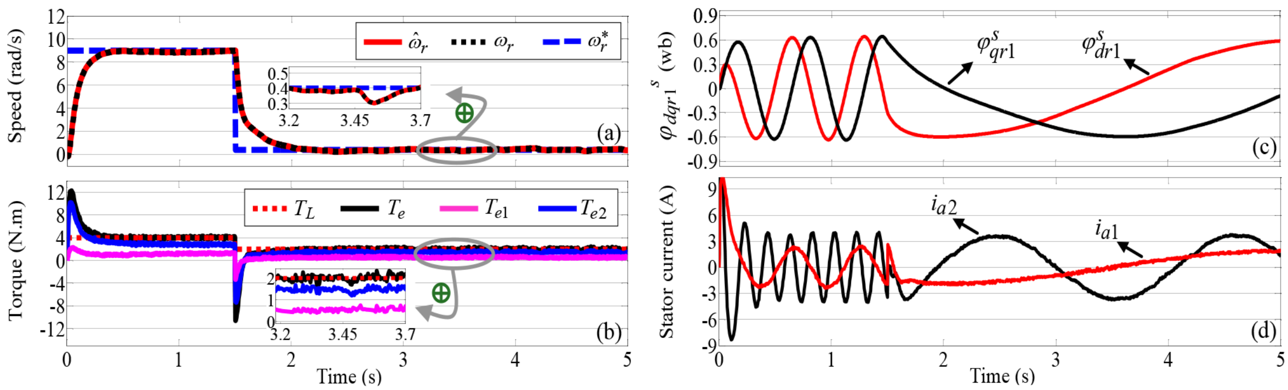

Figure 5. Simulation results of the proposed sensorless DSWIM drive based on MIMRAS as biobjective function. The reference speed changes from 9 to 0.4 rad/s, the load torque drops from 4 to 2 N.m: a) Rotor speed profile, b) Torque profile, c) Estimated rotor fluxes, and d) Stator currents i_{a1} and i_{a2}.

on a classical PI controller at the low reference speed of 2 rad/s. Figure 6b shows the suitable performance of the proposed single-objective intelligent MRAS. Figure 6c shows the high accuracy of the proposed biobjective MRAS at the low reference speed of 2 rad/s in the transient and steady states. Figure 6d demonstrates the suitable behavior of the proposed single-objective intelligent MRAS compared to the proposed MRAS based on a classical PI controller in the steady state. In addition, this figure shows the high accuracy of the biobjective MIMRAS compared to the single-objective MIMRAS in the transient and steady states. In these methods, the speed estimation error $(\hat{\omega}_r - \omega_r)$ is shown in Figure 6e. The proposed biobjective intelligent MRAS has better accuracy compared to other methods at low speed.

4.3. Comparing the simulation results of the proposed control scheme with the conventional method

In Figure 7a, the reference speed is 9 rad/s and the load torque value is 4 N.m. In Figure 7b, the reference speed is 0.4 rad/s and the load torque value is 2 N.m. The torque per ampere ratio (T/I) produced in the DSWIM drive for both the proposed and the conventional methods are shown in Figures 7a$_1$ and 7b$_1$. The proposed method has better T/I ratios compared to the conventional method. As reported in [2], in order to have an appropriate torque-per-ampere ratio in the DSWIM, the motor has to work in its standard operating mode. Figures 7a$_2$ and 7b$_2$ show the sum of the total loss (including conduction and commutation losses) of inverter units in both the proposed and the conventional methods. The proposed method has considerable reduction in losses compared to the conventional method.

The sum of the produced torques in the proposed and conventional methods is equal to the total torque. In the conventional method, it is possible that the produced torque of one of the windings is greater than the total torque. Nevertheless, in the proposed control method, the produced torque of each winding is always smaller than the total torque. For $T_e > 0$, the sum of the absolute value of torques produced in each stator winding $(|T_{e1}| + |T_{e2}|)$ is less in the proposed method than the conventional method. Thus, the improvement in torque-per-ampere ratio and the reduction in total loss of the inverter units for the proposed method compared to the conventional method are expected. In the conventional method, the free hardware capacity of the motor, which normally includes losses, is used. The proposed method has an acceptable performance in terms of inverter loss and increasing its efficiency.

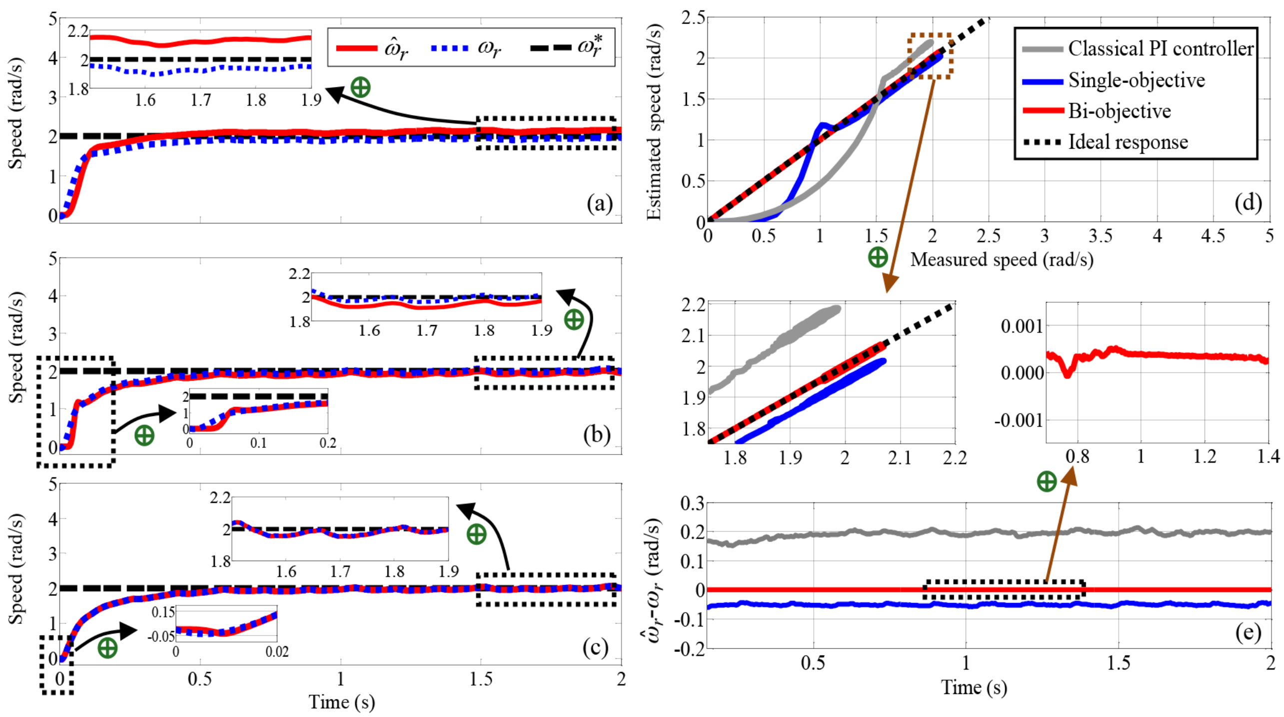

Figure 6. Simulation results of the proposed sensorless DSWIM drive in response to the speed command of 2 rad/s with the load torque value of 1 N.m: a) Rotor speed profile in response to the proposed MRAS based on classical PI controller, b) Rotor speed profile in response to the proposed intelligent MRAS based on single-objective function, c) Rotor speed profile in response to the proposed intelligent MRAS based on biobjective function, d) Comparing the speed estimation accuracy in the proposed methods based on MRAS, and e) Speed estimation error in the proposed methods based on MRAS.

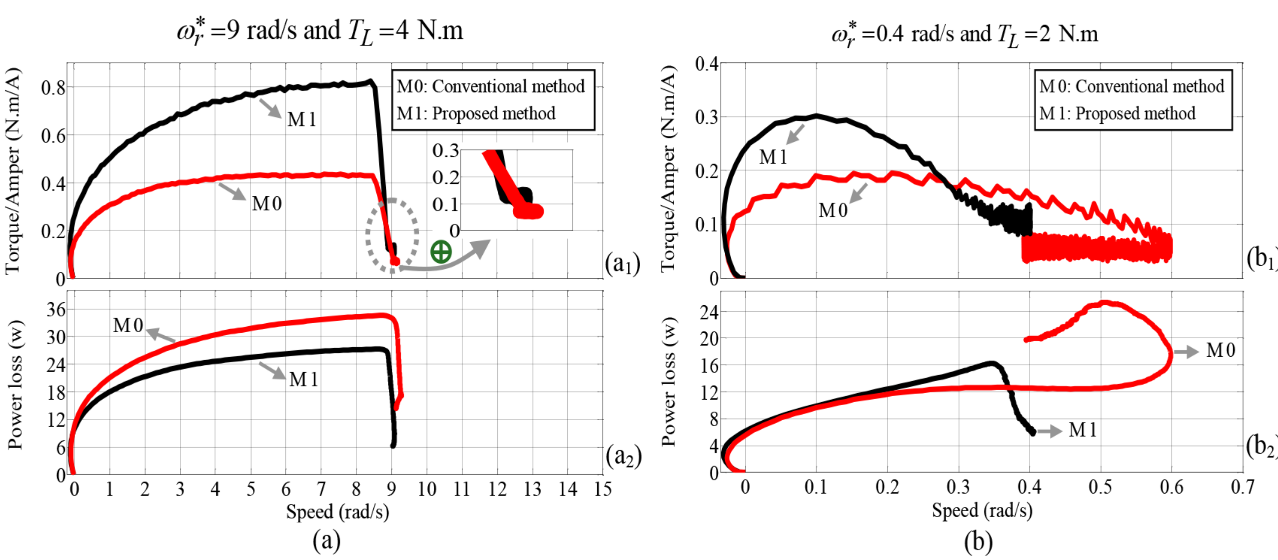

Figure 7. Simulation results of the conventional (M0) and proposed (M1) methods: Torque per ampere ratio (a_1 and b_1) and Sum of the total loss (a_2 and b_2) (including conduction and commutation losses) of DSWIM drive inverter units.

In Figure 8, the percentages of the sum of total loss of commutation and conduction in the inverter units of the DSWIM drive are shown in the proposed method compared to the conventional method for speed commands of 0, 0.4, 3, 6, and 9 rad/s with load torque values of 1, 2, 0, 5, and 4 N.m, respectively. From this figure, it is observed that the proposed control scheme has less power losses in the inverter units compared to the conventional one at very low speeds with the light loads, the loss reduction is significant. In the proposed control scheme, the produced torque of each winding is always smaller than the total torque. As shown in Figure 4, the total torque is equal to 2 N.m, whereas the *abc*1 winding produces more torque than what is requested because of its constant excitation frequency.

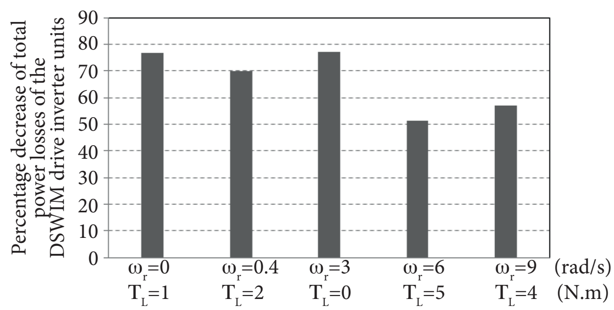

Figure 8. Decreasing the total loss (conduction and commutation losses) of the DSWIM drive inverter units in the proposed method compared to the conventional method for speed commands of 0, 0.4, 3, 6, and 9 rad/s with torque values of 1, 2, 0, 5, and 4 N.m, respectively.

4.4. Robustness of the proposed control scheme to the rotor resistance changes

Figure 9 shows the simulation results of the proposed sensorless DSWIM drive based on MIMRAS as biobjective function for 0 to 60% variations in the rotor resistance. The speed commands are 5 and 10 rad/s with load torque value of 1 N.m. The estimated and actual speed profiles are shown in Figure 9a. These figures show that the sensorless DSWIM drive perfectly traces the low reference speeds in the transient and steady states without any oscillations. The effect of rotor resistance variation on the sensitivity of the estimated rotor fluxes in adaptive model of MIMRAS is shown in Figure 9b. These figures show that the sensitivity percentages of $\hat{\varphi}^s_{dr1}$ and $\hat{\varphi}^s_{qr1}$ to rotor resistance in the adaptive model of the MIMRAS are less than 6% and 4% at speeds of 5 and 10 rad/s, respectively. The estimated rotor-flux hodographs in sensorless DSWIM drive are shown in Figure 9c. Figure 10 shows the simulation results of the proposed sensorless DSWIM drive based on biobjective MIMRAS for 80% variation of the rotor resistance of the DSWIM. In Figure 10, the speed command is 3 rad/s with the load torque value of 1 N.m. In Figures 10a–10d, it is observed that the performance of the proposed sensorless DSWIM drive is suitable for 80% variation of the rotor resistance at low speed. Figure 10f shows that the 80% variation in rotor resistance on the sensitivity of the estimated rotor fluxes in the adaptive model of MIMRAS is less than 7% at the speed of 3 rad/s. In emotional intelligent controller, the K_p and K_i coefficients of PI controller are corrected based on the new value of rotor resistance. In Figures 9 and 10, it is observed that the proposed emotional intelligent controller based on biobjective function has a suitable robustness to variations of the rotor resistance at low speed. The main advantage of the MIMRAS is its small sensitivity to the rotor resistance changes.

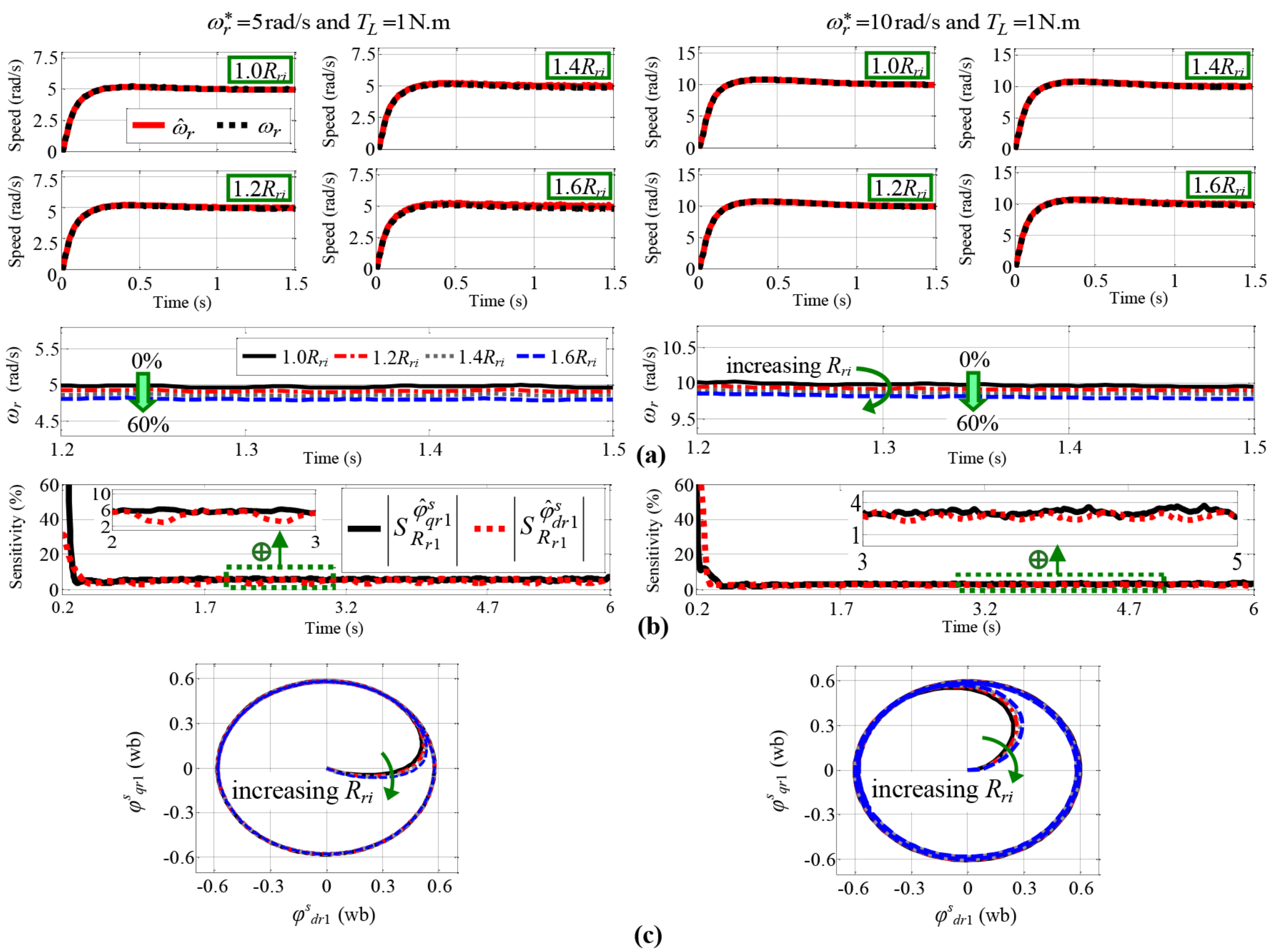

Figure 9. Simulation results of the sensorless DSWIM drive based on biobjective MIMRAS for 0 to 60% variations in rotor resistance. a) Estimated and actual speed profiles, b) The effect of variation in rotor resistance on the sensitivity of the estimated rotor fluxes in adaptive model of MIMRAS, and c) Estimated rotor-flux hodographs.

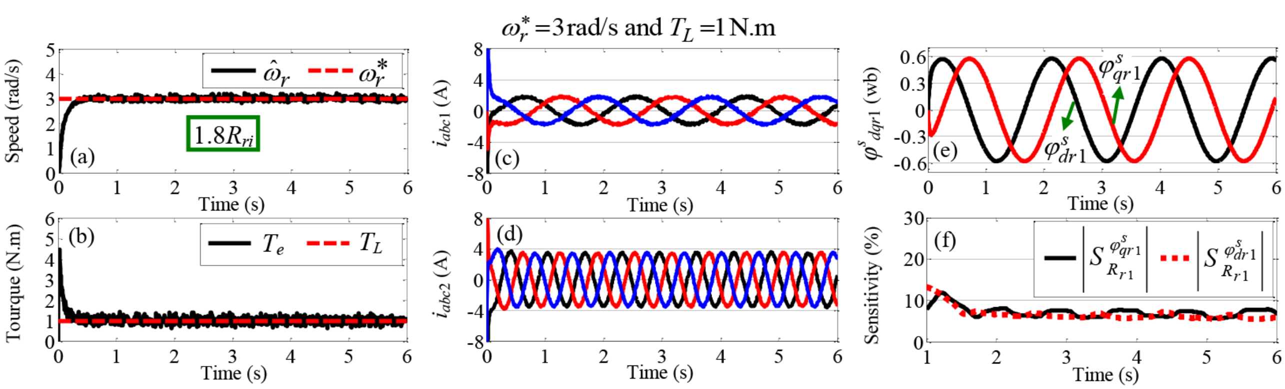

Figure 10. Simulation results of the sensorless DSWIM drive based on biobjective MIMRAS for 80% variation in rotor resistance. a) Estimated and reference speeds profile, b) Load and electromagnetic torque, c and d) Stator currents $abc1$ and $abc2$ windings, e) Estimated rotor fluxes, and f) Sensitivity functions of the adaptive model.

5. Conclusions

This paper presents the modeling of the biobjective brain emotional intelligent controller to improve the performance of the sensorless DSWIM drive at low speed. The DSWIM studied in this paper has a standard squirrel-cage rotor and a stator with two separate three-phase windings with different numbers of poles. In this paper, the following two proposed topics were taken into account:

1. A technique was presented based on the rotor flux compensation in the drive control system of DSWIM that solved the problem of the low rotor flux at low speed and reduced the inverter loss. This idea has two advantages at low speed: 1. It was not essential to estimate the stator resistance, and 2. In the proposed DSWIM drive, the motor worked in its standard operating mode. As a result, power losses in the inverter units were reduced.

2. The modified intelligent MRAS is proposed for the speed estimation, at low speed. In the proposed MIMRAS: 1. An integration algorithm was used instead of pure integrations of reference and adaptive models, 2. The rotor flux components φ^s_{dr} and φ^s_{qr} in the MIMRAS reference model were generated based on the rotor flux compensator idea, and 3. The adaptation algorithm was proposed based on brain emotional learning as single-objective and biobjective functions.

The proposed control scheme has less power losses in the inverter units compared to the conventional one. Simulation results confirmed the superior performance of the proposed sensorless DSWIM drive based on the MIMRAS at low speed.

References

[1] Muñoz AR, Lipo TA. Dual stator winding induction machine drive. IEEE T Ind Appl 2000; 36: 1369-1379.

[2] Guerrero JM, Ojo O. Total air gap flux minimization in dual stator winding induction machines. IEEE T Power Electr 2009; 24:787-795.

[3] Basak S, Chakraborty C. Dual stator winding induction machine: problems, progress and future scope. IEEE T Ind Electron 2015; 62: 4641-4652.

[4] Moayedirad H, Farshad M, Shamsi-Nejad MA. Making robustness and performance improvement of induction motor drive against common variations of motor parameters using intelligent controller based on emotional learning. Journal of Iranian Association of Electrical and Electronics Engineers 2017; 14: 103-118.

[5] Moayedirad H, Shamsi-Nejad MA, Farshad M. Improvement of induction motor drive operation in low and high speeds using rotor flux compensation. Journal of Iranian Association of Electrical and Electronics Engineers 2012; 9: 59-64.

[6] Arunachalam K, Srinivasan H, Muthuramalingam N. A novel NN based rotor flux MRAS to overcome low speed problems for rotor resistance estimation in vector controlled IM drives. Front Energy 2016; 10: 382-392.

[7] Özsoy ES, Gökaşan M, Bogosyan S. Simultaneous rotor and stator resistance estimation of squirrel cage induction machine with a single extended Kalman filter. Turk J Electr Eng Co 2010; 18: 853-863.

[8] İnan R, Barut M. Bi input-extended Kalman filter-based speed-sensorless control of an induction machine capable of working in the field-weakening region. Turk J Electr Eng Co 2014; 22: 588-604.

[9] Aktaş M, Okumuş Hİ. Stator resistance estimation using ANN in DTC IM drives. Turk J Electr Eng Co 2010; 18: 197-210.

[10] Alsofyani IM, Idris NRN. Simple flux regulation for improving state estimation at very low and zero speed of a speed sensorless direct torque control of an induction motor. IEEE T Power Electr 2016; 31: 3027-3035.

[11] Alsofyani IM, Idris NRN. Lookup-table-based DTC of induction machines with improved flux regulation and extended Kalman filter state estimator at low-speed operation. IEEE T Ind Inform 2016; 12: 1412-1425.

[12] Stojic D, Milinkovic M, Veinovic S, Klasnic I. Improved stator flux estimator for speed sensorless induction motor drives. IEEE T Power Electr 2015; 30: 2363-2371.

[13] Samat AAA, Ishak D, Omar AM, Iqbal S, Raza MA. A new speed sensorless field oriented controller for PMSM based on MRAS and PSO. Journal of Electrical Systems 2016; 12: 565-573.

[14] Moutchou M, Abbou A, Mahmoudi H. MRAS-based sensorless speed backstepping control for induction machine, using a flux sliding mode observer. Turk J Electr Eng Co 2015; 23: 187- 200.

[15] Wu Z, Ojo O, Sastry J. High-performance control of a dual stator winding DC power induction generator. IEEE T Ind Appl 2007; 43: 582-592.

[16] Ojo O, Wu Z. Speed control of a dual stator winding induction machine. In: IEEE 2007 20th Applied Power Electronics Conference; 25 Feb.–1 March 2007; Anaheim, CA, USA. New York, NY, USA: IEEE. pp. 229-235.

[17] Novotny DW, Lipo TA. Vector Control and Dynamics of AC Drives. 2nd ed. New York, USA: Oxford University Press Inc., 1997.

[18] Ojo O, Wu Z. Modeling of a dual-stator-winding induction machine including the effect of main flux linkage magnetic saturation. IEEE T Ind Appl 2008; 44: 1099-1107.

[19] Bose BK. Modern Power Electronics and AC Drives. 1st ed. New Jersey, NJ, USA: 2002.

[20] Hu J, Wu B. New integration algorithms for estimating motor flux over a wide speed range. IEEE T Power Electr 1998; 13: 787-795.

[21] Farshad M, Lucas C. Modeling, design and intelligent control of switched reluctance motor (SRM) for washing machine application. PhD, University of Tehran, Tehran, Iran, 2006.

[22] Kowalska TO, Dybkowski M. Stator-current-based MRAS estimator for a wide range speed-sensorless induction-motor drive. IEEE T Ind Electron 2010; 57: 1296-1308.

Appendix

Power Rating = 2 hp, $P_1 = 2$, $P_2 = 6$, $R_{s1} = 3.4\Omega$, $L_{ls1} = 0.006$ H, $R_{r1} = 0.61\ \Omega$, $L_{lr1} = 0.006$ H, $L_{m1} = 0.336$ H, $R_{s2} = 1.9\Omega$, $L_{ls2} = 0.009$ H, $R_{r2} = 0.55\Omega$, $L_{lr2} = 0.009$ H, $L_{m2} = 0.093$ H, $K_1 = 0.333$, $K_2 = 0.6$, $C_1 = 0.01$, $C_2 = 0.001$, $a_{ec1} = 27$, $a_{ec2} = 0.7$, $a_{ec3} = 27$.